Redox-active ligand-mediated assembly for high-performance transition metal oxide nanoparticle-based pseudocapacitors

Jeongyeon Ahn [a,1], Yongkwon Song [a,1], Ye Ji Kim [b], Donghyeon Nam [a], Taewoo Kim [b], Kyungwon Kwak [b], Cheong Hoon Kwon [c], Yongmin Ko [d,*], Suk Joong Lee [b,*], Jinhan Cho [a,e,*]

[a] Department of Chemical and Biological Engineering, Korea University, 145 Anam-ro, Seongbuk-gu, Seoul 02841, Republic of Korea
[b] Department of Chemistry, Korea University, 145 Anam-ro, Seongbuk-gu, Seoul 02841, Republic of Korea
[c] Division of Energy Engineering, Kangwon National University, 346 Jungang-ro, Samcheok 25913, Republic of Korea
[d] Division of Energy Technology, Materials Research Institute, Daegu Gyeongbuk Institute of Science and Technology (DGIST), 333 Techno Jungang-daero, Hyeonpung-eup, Dalseong-gun, Daegu 42988, Republic of Korea
[e] KU-KIST Graduate School of Converging Science and Technology, Korea University, 145 Anam-ro, Seongbuk-gu, Seoul 02841, Republic of Korea

ABSTRACT

The important issues in preparing transition metal oxide nanoparticle (TMO NP)-based energy storage electrodes, such as pseudocapacitor electrodes, are to effectively minimize the amount of electrochemically inactive organics (i.e., polymeric binders and ligands stabilizing NPs) and simultaneously increase the amount of high-energy TMO NPs within a limited electrode area/volume without a significant loss in charge transfer kinetics. Herein, we introduce a redox-active ligand-mediated layer-by-layer (LbL) assembly as a novel approach for significantly enhancing the energy storage performance of TMO NP-based pseudocapacitor electrodes. In this study, high-energy TMO NPs and conductive NPs are periodically LbL-assembled using redox-active porphyrin ligands instead of polymeric binders. During LbL deposition, the insulating native ligands on the NP surface are successfully exchanged with carboxylic acid-functionalized porphyrin ligands, forming a densely NP-packed structure that can minimize the mass and volume of electrochemically inactive components. Based on this redox-active ligand-mediated LbL approach, the resultant pseudocapacitor electrodes exhibit much higher energy capacities (areal, volumetric, and specific capacities) and superior rate capability than insulating polymeric ligand-mediated electrodes as well as previously reported electrodes. Our approach can provide a fundamental basis for fully exploiting the energy efficiency of components and further designing a variety of high-performance electrochemical electrodes.

1. Introduction

The recent rapid growth and expansion in the use of electric vehicles and wearable/portable electronic devices have strongly necessitated the development of energy storage devices with more advanced electrochemical performance (i.e., higher energy/power densities and longer operation lifetime) than the existing devices [1–5]. Generally, the high energy density of energy storage devices can be achieved by densely loading high-energy active materials in a limited electrode area/volume [6,7]. In particular, pseudocapacitive transition metal oxide nanoparticles (TMO NPs) with reversible Faradaic reactions and a large

active surface-to-volume ratio have been considered as one of the most promising active components that can resolve the low energy density issue of conventional carbonaceous material-based supercapacitors and further reduce the large gap in the energy density between supercapacitors and lithium-ion batteries [8,9]. However, the inherently poor electrical properties of TMO NPs as well as the numerous interfacial resistance sites between neighboring NPs seriously impede the electron transfer within the electrodes, limiting the practical output of their high theoretical capacitance (i.e., low energy efficiency) [10–13]. Additionally, the insulating organic ligands bound to the surface of TMO NPs act as other major interfacial resistance sites, which imposes a limit on

effectively deriving the intrinsic energy properties of TMO NPs [14]. As a result, the use of TMO NPs inevitably causes a trade-off between energy density and power density, which becomes more problematic at a higher loading amount (i.e., electrode thickness) of TMO NPs for higher energy density [7,8].

Along with the aforementioned critical issues, polymeric binders and carbonaceous conductive enhancers, which have been widely used as essential components in conventional slurry-based electrode fabrication methods, should also be seriously considered with regard to energy storage performance. That is, since those bulky components (i.e., polymeric binders and carbonaceous conductive enhancers) occupy a significant portion of the limited area/volume of electrodes, they can directly or indirectly affect the charge transfer kinetics within the electrodes and consequently have adverse effects on the overall electrochemical performance of electrodes [15–18]. Specifically, the insulating polymeric binders providing the mechanical integrity of electrodes by strongly binding each component restrict the facile electron communication at the interfaces between active components, resulting in a decrease in the energy efficiency and rate capability [16,17]. Additionally, the use of bulky carbonaceous conductive enhancers (e.g., carbon nanotubes and/or reduced graphene oxides) for better electron transfer can lead to poor volumetric performance due to the formation of electrodes with low packing densities [18]. Furthermore, simple physical blending between those additive components and active materials without a sufficient understanding of interfacial interactions is highly vulnerable to the partial segregation/agglomeration of electrode components, which act as 'inactive dead mass/volume' in electrodes [19]. From this point of view, if these essential but electrochemically inactive and/or bulky components can be properly replaced with unique electrode components that can induce more facile charge transfer and higher energy density through favorable interfacial interactions, the areal/volumetric/specific capacities, rate capability, and operational stability of the resulting electrodes can be notably enhanced.

Herein, we introduce a novel approach (i.e., redox-active ligand-mediated layer-by-layer (LbL) assembly) that can significantly enhance the energy storage performance of TMO NP-based pseudocapacitor electrodes without electrochemically inactive organic species (i.e., polymeric binders and/or native ligands bound to the NP surface). A notable advantage of our approach is that the porphyrins act as redox-active ligands (or linkers) that can directly and robustly integrate all electrode components, thereby improving the areal/volumetric/specific capacities while maintaining good rate capability and structural stability. To our knowledge, there have been few studies for converting electrochemically inactive organic ligands to the redox-active ligands bound to the surface of active components including TMO NPs.

Particularly, the porphyrins (or their related structures) have been studied as promising electrochemically active organic materials based on their unique electrochemical characteristics (i.e., facile electron uptake/release properties due to the small highest occupied molecular orbital (HOMO)–lowest unoccupied molecular orbital (LUMO) gap and high electrochemical activity due to the redox reactions mediated by the conjugated π electrons on the macrocycle ring) [20–25]. However, most porphyrin-based electrodes reported to date have focused only on the electrochemical activity of porphyrins, thereby inevitably requiring the use of insulating polymeric binders in the electrode preparation [25–28]. On the other hand, it is worth noting that the porphyrins in our study are interface-modified to be employed as redox-active ligands bound to the surface of TMO NPs. Specifically, our approach is characterized by the fact that carboxylic acid (COOH)-functionalized porphyrin ligands are directly assembled with high-energy TMO NPs and conductive NPs through *in situ* ligand exchange reaction between the porphyrin ligands and the native ligands on the surface of NPs. That is, the porphyrins in our system operate not only as an electrochemically active material for additional energy capacity but also as a ligand (or linker) that robustly connects all components in the electrodes based on well-defined interfacial interactions. In particular, our approach can

provide a homogeneously and densely NP-packed structure that enables facile charge transfer at all interfaces within the electrodes, minimizing the presence of inactive dead mass/volume (i.e., partially agglomerated parts and excess large pores) even at high electrochemical sweep rates.

For this study, Mn(III)-porphyrin bis-carboxylic acid (MnPP) with high electrochemical activity was used as a redox-active ligand for the LbL assembly of high-energy iron oxide (Fe_3O_4) NPs and conductive indium tin oxide (ITO) NPs (Scheme 1). In this case, oleic acid (OA) and/or oleylamine (OAm) ligands loosely bound to the surface of Fe_3O_4 and ITO NPs were readily replaced by the MnPP ligands during consecutive LbL deposition due to the higher interfacial affinity (i.e., coordination binding) between the carboxylic acid (COOH) groups of MnPP ligands and the surface of NPs, resulting in a robust electrode structure. Additionally, the conductive ITO NPs were incorporated into the Fe_3O_4 NP array to form a homogeneous and nanoblended conductive network, along with semiconducting porphyrin ligands, which could further enhance the charge transfer kinetics of the electrodes. As a result, the formed (Fe_3O_4 NP/MnPP/ITO NP/MnPP)$_m$ electrodes (m: periodic number for the LbL assembly) exhibited a remarkably higher capacity, better rate capability, and longer operational stability compared to insulating polymeric-incorporated electrodes. In addition, when our approach was applied to porous textile-type current collectors (TCCs) with a large specific surface area, all electrode components could be conformally coated onto the entire region ranging from the exterior to the interior of the TCC without blocking its inherent pores, delivering a high areal performance of ~2.1 F cm^{-2} (at a current density of 3.0 mA cm^{-2}) at a high mass loading of ~9.8 mg cm^{-2} and outperforming the previously reported Fe_3O_4-based electrodes [29–36]. We believe that our approach for the structural design and interfacial interactions based on redox-active ligand-mediated LbL assembly can provide a basis for developing and designing high-performance energy storage devices.

2. Results and discussion

2.1. MnPP-mediated assembly of high-energy TMO NPs and conductive NPs

To use porphyrin as a redox-active ligand (or linker) bridging the interfaces between adjacent NPs (Fig. 1a-1b), we first synthesized MnPP molecules with COOH groups attached to both sides of macrocycle ring (i.e., the *para*-positions of pyrrole ring). The as-prepared MnPP with COOH groups showed a stable dispersion in ethanol, and its UV–vis absorption spectrum indicated the typical Soret band (at 478 nm) and Q band (at 580–620 nm) originating from the electronic transition between porphyrin and Mn(III) core orbitals (Fig. S1a) [37–39]. In this case, the COOH groups of MnPP not only provide favorable interfacial interactions that can induce the formation of a robust electrode structure but also impart the hydrophilic properties to all exposed surface of NPs within the electrodes, enabling an excellent interfacial wettability in aqueous electrolytes for facile ion diffusion (the more details are given in the later part). In addition, the organic MnPP molecules exhibited a low molecular weight (M_w) of ~931 g mol^{-1} and an amorphous structure as confirmed by X-ray diffraction (XRD) analysis (Fig. S1b-S1c). Particularly, as shown in the electron configuration and corresponding frontier orbital diagram using density functional theory (DFT) (Fig. S2), the neutral MnPP molecules possessed a small HOMO–LUMO gap of ~2.06 eV [40], allowing facile electron uptake/release properties for the enhanced charge transfer kinetics within the electrodes.

To fabricate TMO NP-based pseudocapacitor electrodes using the MnPP ligands, we prepared OA-Fe_3O_4 NPs with a diameter of ~7 nm as high-energy TMO NPs and OAm-ITO NPs with a diameter of ~9 nm as conductive NPs *via* solvothermal reactions, which displayed a high dispersion stability in toluene and well-defined crystalline structures (Fig. 1a and Fig. S3) [41,42]. Given that the structural characteristics (i. e., high crystallinity, grain boundary, and narrow size distribution) of TMO NPs significantly affect the electrochemical behaviors, the
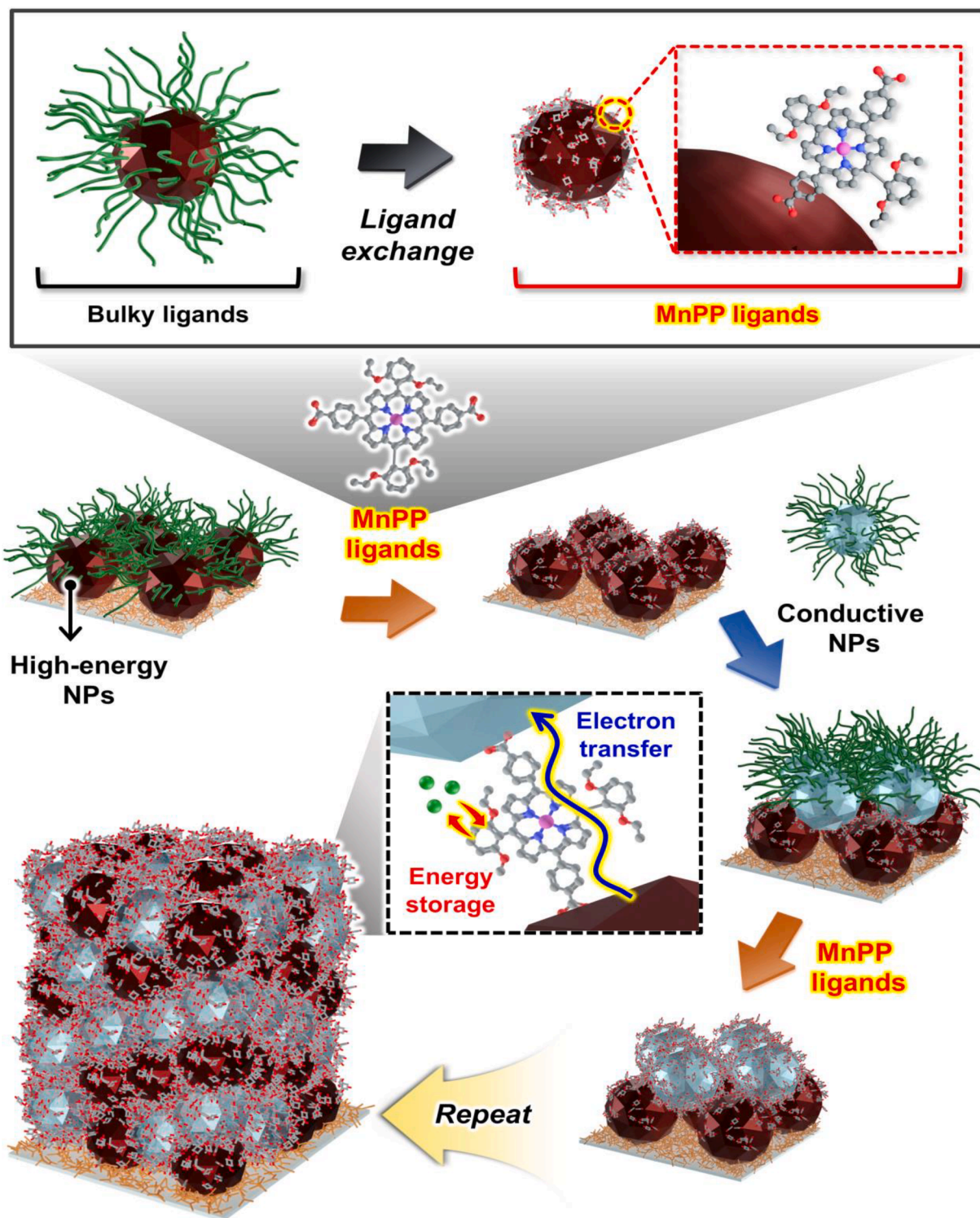
Scheme 1. Schematic representation for the MnPP-mediated LbL assembly of TMO NP-based pseudocapacitor electrodes with a densely packed and nanoblended internal structure.

synthesized OA-Fe$_3$O$_4$ NPs in our work can deliver better energy storage performance than bulk Fe$_3$O$_4$ [14,43,44]. As already mentioned above, the COOH groups of MnPP ligands had a high interfacial affinity to the bare surface of Fe$_3$O$_4$ and ITO NPs, which was clearly confirmed by Fourier transform infrared (FTIR) spectroscopy in an advanced grazing angle (AGA) specular mode during consecutive LbL assembly. In the FTIR spectra, the MnPP exhibited strong C—H stretching peaks (assigned to the macrocycle ring) at 2924 and 2854 cm^{-1}, where the

pristine OA-Fe$_3$O$_4$ and OAm-ITO NPs displayed the same absorption peaks originating from the long aliphatic chains of native OA/OAm ligands (Fig. S4). Therefore, the adsorption behaviors of MnPP ligands were investigated by monitoring their typical absorption peaks (i.e., aromatic C—N (at 1244 cm^{-1}), in-plane C—H (at 1086 cm^{-1}), and Mn-N (at 1011 cm^{-1}) vibrations) that did not overlap with those of native OA/OAm ligands (Fig. S4c) [45]. Specifically, when the MnPP was assembled onto the OA-Fe$_3$O$_4$ NP-coated substrate (see the MnPP/Fe$_3$O$_4$ NP in
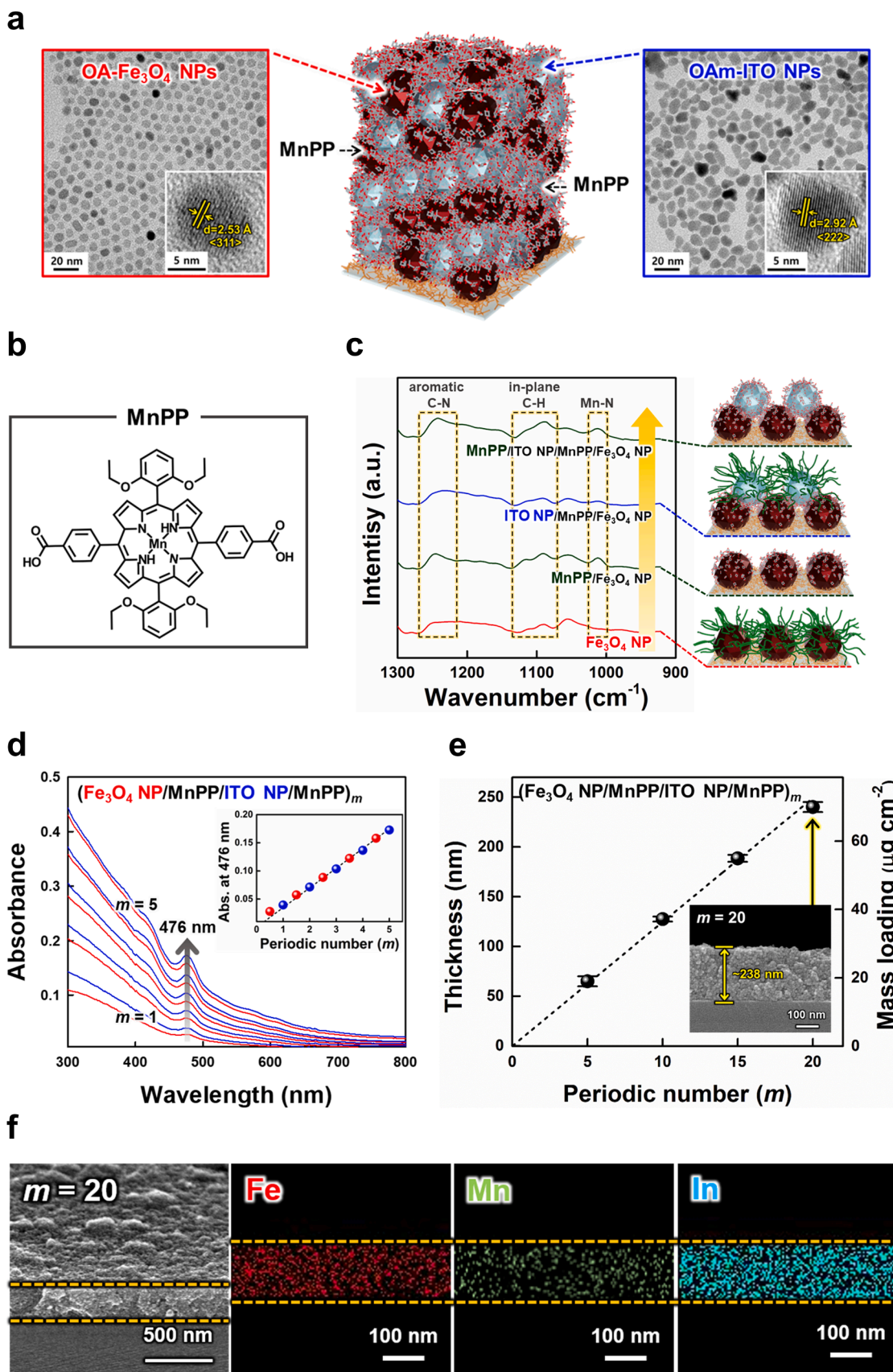
(caption on next page)

Fig. 1. (a) Schematic diagram of the multilayers composed of OA-Fe_3O_4 NPs, OAm-ITO NPs, and MnPP ligands, and HR-TEM images of 7 nm-sized OA-Fe_3O_4 NPs and 9 nm-sized OAm-ITO NPs. The insets of the HR-TEM images indicate the lattice fringe spacing (*d*) and corresponding crystal plane of each NP. (b) Molecular structure of MnPP with COOH groups at the *para*-positions of pyrrole ring. (c) FTIR spectra and schematic representation of (Fe_3O_4 NP/MnPP/ITO NP/MnPP)$_m$ multilayers obtained by sequentially depositing each layer. The outermost layer is represented as a red line for Fe_3O_4 NP, a blue line for ITO NP, and a green line for MnPP. (d) UV–vis absorbance spectra and absorbance at a wavelength of 476 nm (inset) of (Fe_3O_4 NP/MnPP/ITO NP/MnPP)$_m$ multilayers as the periodic number increases from 1 to 5. The red line/circles and blue line/circles indicate the deposition of (Fe_3O_4 NP/MnPP) and (ITO NP/MnPP), respectively. (e) Film thickness (left axis) and mass loading (right axis) of (Fe_3O_4 NP/MnPP/ITO NP/MnPP)$_m$ multilayers as a function of the periodic number, which were obtained from cross-sectional FE-SEM images and quartz crystal microbalance (QCM) measurements, respectively. The inset shows the cross-sectional FE-SEM image with a film thickness of ~238 nm at the periodic number of 20. (f) Tilted FE-SEM image and corresponding EDS elemental mapping images of (Fe_3O_4 NP/MnPP/ITO NP/MnPP)$_{20}$ multilayers. (For interpretation of the references to colour in this figure legend, the reader is referred to the web version of this article.)

Fig. 1c), the absorption peaks of MnPP were intensified due to the strong interfacial interactions (i.e., coordination bonding) between the multiple COOH groups of MnPP and the surface of Fe_3O_4 NPs [46]. When OAm-ITO NPs were sequentially deposited onto the MnPP/Fe_3O_4 NP/ substrate (see the ITO NP/MnPP/Fe_3O_4 NP in Fig. 1c), the absorption peaks of MnPP were reduced again, suggesting that the ITO NPs were densely coated through the abovementioned coordination bonding-induced LbL deposition. In this case, the MnPP ligands with multiple COOH groups could act as multidentate ligands for oxide NPs, thereby providing a robust electrode structure [47]. That is, the MnPP-mediated LbL assembly could be accomplished by replacing the native OA/OAm ligands (serving as mono- or bidentate ligands) bound to the bare surface of oxide NPs with the multiple COOH groups of MnPP ligands (serving as multidentate ligands). This adsorption mechanism was also supported through the FTIR analysis for COOH-functionalized poly(acrylic acid) (PAA)-mediated LbL assembly, clearly demonstrating the ligand replacement reaction between the native OA/OAm ligands and the multiple COOH moieties (Fig. S5). Furthermore, the periodic oscillation of water contact angles during the LbL assembly of (Fe_3O_4 NP/MnPP/ ITO NP/MnPP)$_m$ multilayers indicated the repetitive ligand replacement reactions, as confirmed in the FTIR analysis. Specifically, when the MnPP layer was deposited onto the NP layer, the water contact angles were significantly decreased from ~98° (for the outermost OA-Fe_3O_4 NP layer) and ~102° (for the outermost OAm-ITO NP layer) to ~64° (for the outermost MnPP layer) (Fig. S6), which implied the possibility of hydrophilic interfacial properties that can facilitate the infiltration of aqueous electrolytes into the electrodes.

Based on the high interfacial interactions between MnPP ligands and oxide NPs, the heterostructured (Fe_3O_4 NP/MnPP/ITO NP/MnPP)$_m$ multilayers were prepared by consecutive LbL assembly. In this case, the vertical growth of the multilayers was investigated using UV–vis spectroscopy and field-emission scanning electron microscopy (FE-SEM) (Fig. 1d-1e and Fig. S7). With increasing the periodic number (*m*), the absorbance at the characteristic peak (λ ~476 nm for the Soret band) of the assembled MnPP ligands (see the inset in Fig. 1d) and the total film thickness (or mass loading) increased almost linearly, implying the uniform and vertical growth of multilayers. Additionally, the mass fraction of each component within the multilayer composites was calculated to be ~34.3 % for Fe_3O_4 NPs, 60.8 % for ITO NPs, and 4.9 % for MnPP through inductively coupled plasma-mass spectrometry (ICP-MS) (Fig. S8). Particularly, given that the film thickness of (Fe_3O_4 NP/ MnPP/ITO NP/MnPP)$_{20}$ multilayers was ~238 nm, the average film thickness per periodic layer was estimated to be ~12 nm, which was smaller than the total diameters of the incorporated oxide NPs (i.e., 7 nm-sized Fe_3O_4 NPs and 9 nm-sized ITO NPs). This phenomenon implied that the formed multilayers possessed a nanoblended internal structure rather than a highly ordered structure with stratified interfaces, which was also observed in cross-sectional FE-SEM and energy-dispersive X-ray spectroscopy (EDS) elemental mapping images (Fig. 1f). This nano-blended structure is very important in that the homogeneous distribution of conductive ITO NPs throughout the entire electrode region can induce a well-interconnected electron network to effectively lower the internal resistance of electrodes. It should also be noted that the (Fe_3O_4 NP/MnPP/ITO NP/MnPP)$_m$ multilayers exhibited a densely NP-packed structure with a high mass density of ~2.9 g cm^{-3} without the

aggregations of components (Fig. S9). The numerous nanopores generated among neighboring NPs were maintained even after consecutive LbL assembly, possibly providing sufficient ion diffusion pathways during successive electrochemical sweeps. Additionally, to investigate the physical adhesion stability of (Fe_3O_4 NP/MnPP/ITO NP/MnPP)$_{20}$ multilayers on substrates, we conducted the peeling test using a 3 M adhesive tape (Fig. S10). After peeling off the 3 M tape attached to the multilayers, there was no apparent delamination from the substrate, indicating that the multilayers were stably deposited with strong interfacial interactions (i.e., coordination bonding) between the COOH groups of MnPP ligands and the surface of oxide NPs. Considering that the conventional slurry-based electrodes containing polymeric binders and bulky carbonaceous conductive enhancers have much difficulty in sufficiently utilizing the advantages of TMO NPs with large specific surface area due to the low packing density and the aggregations of NPs caused by the unfavorable interfacial interactions [48,49], our approach can provide an efficient way to design robustly structured TMO NP-based pseudocapacitor electrodes with facile charge transfer and high energy capacity.

2.2. Electrochemical properties of MnPP-mediated TMO NP-based electrodes

Based on these results, we examined the electrochemical properties of MnPP ligands in an aqueous 0.5 M Na_2SO_3 electrolyte-based three-electrode system. For this investigation, the COOH-functionalized MnPP ligands were LbL-assembled with conductive ITO NPs onto fluorine-doped tin oxide (FTO) substrates (i.e., (ITO NP/MnPP)$_{20}$ electrode) (Fig. 2a). In this case, the (ITO NP/MnPP)$_{20}$ electrode was prepared without pseudocapacitive Fe_3O_4 NPs for clearly understanding the charge storage behaviors of only MnPP ligands. As a comparative control sample, the COOH-functionalized PAA ligands without any electrochemical activity were also LbL-assembled with the same ITO NPs (i. e., (ITO NP/PAA)$_{20}$ electrode). These electrodes prepared by using two different kinds of linkers also displayed a densely NP-packed surface morphology with similar film thicknesses (Fig. S11).

In the case of CV curves at a scan rate of 100 mV s^{-1} in the negative potential window of −0.9 to 0 V (*vs* Ag/AgCl) (Fig. 2b), the (ITO NP/ PAA)$_{20}$ electrode showed only a quasi-rectangular shape without any noticeable redox peak, implying typical electric double-layer capacitor (EDLC) behaviors originating from conductive ITO NPs [42,50]. In contrast, the (ITO NP/MnPP)$_{20}$ electrode exhibited an evident reversible redox pair at −0.52/−0.34 V along with the EDLC behaviors of ITO NPs. Particularly, the other redox pair at 0.22/0.33 V was also observed in the positive potential window ranging from 0 to 0.9 V (Fig. S12). These redox reactions could be explained by the reversible two conjugated π electron-mediated oxidation and reduction of neutral MnPP (18 π), forming dicationic MnPP^{2+} (16 π) and dianionic MnPP^{2-} (20 π), respectively (Fig. S13) [20]. As a result, the MnPP ligands could be electrochemically operated in both negative and positive potential windows. Additionally, since Fe_3O_4-based electrodes are known to have stable and reversible redox reactions in the negative potential window [51], the electrochemical tests for this study were carried out in the negative potential window to induce a synergistic effect between MnPP ligands and Fe_3O_4 NPs. Furthermore, in the negative CV scan range,
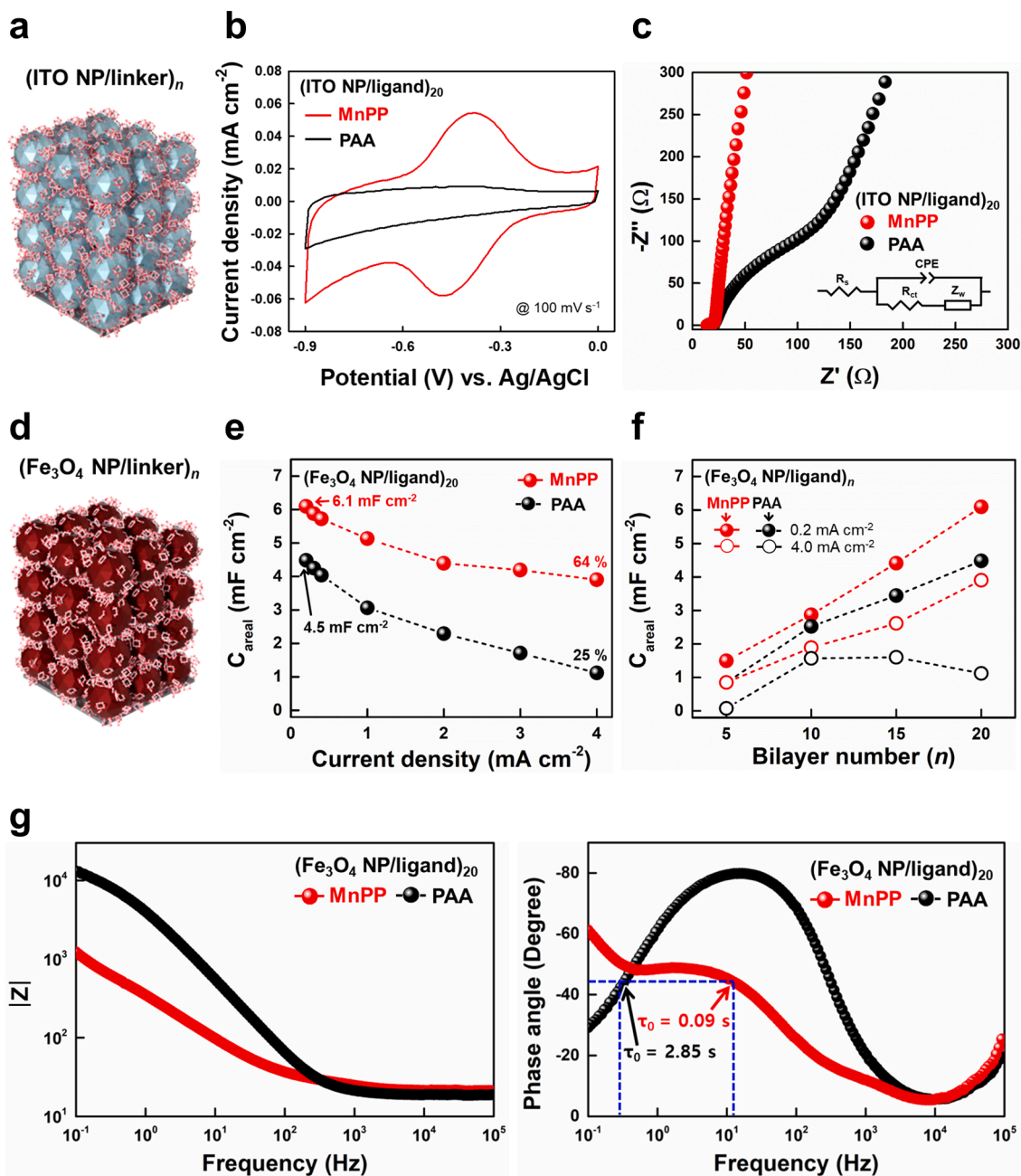
Fig. 2. (a) Schematic diagram of (ITO NP/ligand)$_n$ electrodes. (b) CV curves (at a scan rate of 100 mV s^{-1}) and (c) Nyquist plots with equivalent circuit (inset) of (ITO NP/MnPP)$_{20}$ and (ITO NP/PAA)$_{20}$ electrodes. (d) Schematic diagram of (Fe$_3$O$_4$ NP/ligand)$_n$ electrodes. (e) Areal capacitances (C$_{areal}$) of (Fe$_3$O$_4$ NP/MnPP)$_{20}$ and (Fe$_3$O$_4$ NP/PAA)$_{20}$ electrodes obtained from the GCD measurements with increasing the current density from 0.2 to 4.0 mA cm^{-2}. (f) Bilayer number-dependent of C$_{areal}$ of (Fe$_3$O$_4$ NP/ligand)$_n$ electrodes obtained from the GCD curves at current densities of 0.2 and 4.0 mA cm^{-2} The red and black line/circles represent the (Fe$_3$O$_4$ NP/MnPP)$_n$ and (Fe$_3$O$_4$ NP/PAA)$_n$ electrodes, respectively. (g) Frequency-dependent resistance and phase angle of Bode plots for (Fe$_3$O$_4$ NP/MnPP)$_{20}$ and (Fe$_3$O$_4$ NP/PAA)$_{20}$ electrodes. (For interpretation of the references to colour in this figure legend, the reader is referred to the web version of this article.)

there was no irreversible reaction that could be caused by the over-oxidation and/or polymerization of MnPP ligands [52,53], which was highly advantageous for maintaining the robust electrode structure under successive potential sweeps.

Based on the electrochemical behaviors, when the total charge densities (in a unit of mC cm^{-2}) were obtained from the integrated CV area, the (ITO NP/MnPP)$_{20}$ electrode exhibited a 3.2 times higher value (2.5×10^{-2} mC cm^{-2}) compared to the (ITO NP/PAA)$_{20}$ electrode (7.9×10^{-3} mC cm^{-2}), indicating that the MnPP ligands contributed to the charge storage capacity. It was also worth noting that the MnPP ligands with semiconducting properties could promote the electron transfer kinetics at all the interfaces between adjacent ITO NPs. To confirm this

possibility, electrochemical impedance spectroscopy (EIS) analysis for each electrode was conducted in the frequency range from 10^5 Hz to 0.1 Hz at a potential amplitude of 5 mV using Randles circuit as a model system (Fig. 2c). In this case, the fitted values of equivalent series resistance (ESR) and charge transfer resistance (R$_{ct}$) of the (ITO NP/MnPP)$_{20}$ electrode were measured to be ~14.8 and 6.1 Ω, respectively, which were much lower than those of the (ITO NP/PAA)$_{20}$ electrode (ESR of ~19.9 Ω and R$_{ct}$ of ~86.5 Ω). Furthermore, the (ITO NP/MnPP)$_{20}$ electrode showed much better ion diffusion behaviors with a smaller Warburg impedance coefficient (σ_w) of ~55.4 Ω s$^{-0.5}$ than that of the (ITO NP/PAA)$_{20}$ electrode (~434.9 Ω s$^{-0.5}$) (Fig. S14). These results implied that the MnPP-mediated electrode retained numerous

nanopores among neighboring NPs, thereby facilitating the mass transport in the electrode. With the aid of this enhanced charge transfer kinetics, the (ITO NP/MnPP)$_{20}$ electrode exhibited an almost linear increase in anodic/cathodic peak current densities (i_p, in mA cm^{-2}) as well as negligible peak separation (ΔE_p, ~0.12 mV for 30 mV s^{-1} and ~0.18 mV for 500 mV s^{-1}) even with increasing the scan rate up to 500 mV s^{-1} (Fig. S15), which demonstrated the good charge conduction behaviors of the MnPP ligands.

For better understanding the improved charge transfer behaviors by the MnPP ligands, we then prepared the MnPP-mediated electrode using poorly conductive but pseudocapacitive Fe$_3$O$_4$ NPs without the use of conductive ITO NPs (i.e., (Fe$_3$O$_4$ NP/MnPP)$_{20}$ electrode) (Fig. 2d), and its electrochemical performance was compared with the PAA-mediated electrode (i.e., (Fe$_3$O$_4$ NP/PAA)$_{20}$ electrode). In this case, the MnPP- and PAA-mediated electrodes showed a mass loading of Fe$_3$O$_4$ NPs of approximately 24.0 μg cm^{-2}, which also possessed a densely NP-packed structure (Fig. S16). As confirmed in Fig. 2e, the (Fe$_3$O$_4$ NP/MnPP)$_{20}$ electrode exhibited much higher areal capacitance (C$_{areal}$; calculated from galvanostatic charge/discharge (GCD) profiles) of ~6.1 mF cm^{-2} than the (Fe$_3$O$_4$ NP/PAA)$_{20}$ electrode (C$_{areal}$ of ~4.5 mF cm^{-2}) at the same current density of 0.2 mA cm^{-2}. Importantly, the (Fe$_3$O$_4$ NP/MnPP)$_{20}$ electrode maintained ~64 % of its initial capacitance at a high current density of 4.0 mA cm^{-2}, while the (Fe$_3$O$_4$ NP/PAA)$_{20}$ electrode maintained only ~25 % of its initial value. These results clearly indicated that the MnPP-mediated electrode could exhibit the superior charge transfer behaviors compared to the polymeric ligand-mediated electrode.

In particular, the C$_{areal}$ of the (Fe$_3$O$_4$ NP/MnPP)$_n$ electrodes were almost linearly increased with increasing the bilayer number (n) (or mass loading), even at a high current density (Fig. 2f and Fig. S17). In contrast, the (Fe$_3$O$_4$ NP/PAA)$_n$ electrodes showed considerable difficulty in efficiently utilizing the active Fe$_3$O$_4$ NPs, especially at a high current density as the bilayer number was increased. These results clearly suggested that the insulating polymeric ligands significantly restrict the electronic and/or ionic conductions within the electrodes when the active TMO NPs were deposited with a high mass loading for achieving higher energy density. These phenomena could also be confirmed by the Bode plots from EIS measurements (Fig. 2g). Specifically, the frequency-dependent impedance plots showed that the overall impedance of the (Fe$_3$O$_4$ NP/MnPP)$_{20}$ electrode was approximately 10 times lower than that of the (Fe$_3$O$_4$ NP/PAA)$_{20}$ electrode. Furthermore, the relaxation time constant ($\tau_0 = 1/f_k$, where f_k indicates the knee frequency at a phase angle of $-45°$) of the (Fe$_3$O$_4$ NP/MnPP)$_{20}$ electrode (0.09 s at 10.6 Hz) was much lower than that of the (Fe$_3$O$_4$ NP/PAA)$_{20}$ electrode (2.85 s at 0.35 Hz), evidently indicating that the MnPP ligands could significantly improve the charge transfer kinetics of the electrode, thereby enabling superior rate capability.

On the basis of these results, we designed an electrode structure with higher energy efficiency and more improved rate capability through periodically controlled MnPP-mediated LbL assembly of high-energy Fe$_3$O$_4$ NPs and conductive ITO NPs (i.e., (Fe$_3$O$_4$ NP/MnPP/ITO NP/MnPP)$_m$ electrodes) (see Fig. 1a). As shown in Fig. 3a, the (Fe$_3$O$_4$ NP/MnPP/ITO NP/MnPP)$_m$ electrodes displayed the typical pseudocapacitive behaviors with asymmetric CV curves, resulting from the reversible redox reactions of active materials (i.e., Fe$_3$O$_4$ NPs and MnPP). With increasing the periodic number from 5 to 20, the areal current responses and corresponding integrated area of the (Fe$_3$O$_4$ NP/MnPP/ITO NP/MnPP)$_m$ electrodes gradually increased without a notable shape distortion. Such reversible pseudocapacitive behaviors of the electrodes could also be observed under continuous CV sweeps at various scan rates ranging from 5 to 200 mV s^{-1} (Fig. 3b and Fig. S18), showing the stable electrochemical reactions without any significant overpotential region over the entire potential range. It should also be noted that the (Fe$_3$O$_4$ NP/MnPP/ITO NP/MnPP)$_m$ electrodes exhibited much higher current responses compared to the conventional slurry-casted electrode composed of the same mass loading of active materials (i.e., Fe$_3$O$_4$ NP

and MnPP), which was mainly attributed to the rational structure and interfaces as mentioned above (Fig. S19).

In addition, the C$_{areal}$ of the (Fe$_3$O$_4$ NP/MnPP/ITO NP/MnPP)$_m$ electrodes obtained from the GCD measurements (at various current densities ranging from 0.2 to 4.0 mA cm^{-2}) was linearly increased with increasing the periodic number from 5 to 20 (Fig. 3c and Fig. S20 – S22). In this case, the (Fe$_3$O$_4$ NP/MnPP/ITO NP/MnPP)$_{20}$ electrode delivered C$_{areal}$ of ~8.4 mF cm^{-2} at a current density of 0.2 mA cm^{-2}, and maintained ~72.6 % of the value even at a high current density of 4.0 mA cm^{-2}, indicating the high energy efficiency and excellent rate capability (see Fig. 3c). Importantly, the specific capacitances (C$_{specific}$; calculated from the total mass of the electrodes) were almost maintained from ~129.9 F g^{-1} ($m = 5$) to ~125.1 F g^{-1} ($m = 20$) (see Fig. S22), suggesting an efficient electrode structure of the MnPP-mediated system. These phenomena were further confirmed by the EIS measurements that the resistances of the electrodes exhibited a negligible change despite the increase in periodic number (related to the film thickness) (Fig. S23). In contrast, the polymeric ligand-mediated electrode (i.e., (Fe$_3$O$_4$ NP/PAA/ITO NP/PAA)$_{20}$ electrode) showed a relatively lower C$_{areal}$ of ~5.8 mF cm^{-2} in the GCD curve at a current density of 0.2 mA cm^{-2} (Fig. 3d) although the mass loading of each NP (i.e., Fe$_3$O$_4$ and ITO NPs) within the PAA-mediated electrode was adjusted to be almost the same as that within the MnPP-mediated electrode. Particularly, considering that the capacitance contribution of MnPP ligands was estimated to be ~3.9 % (calculated from both the mass fraction of MnPP ~ 4.9 % and the experimentally measured specific capacitance of ~98 F g^{-1}) (see Fig. S8 and Fig. S24), it is highly reasonable to conclude that these notable enhancements in the specific/areal capacitances of the (Fe$_3$O$_4$ NP/MnPP/ITO NP/MnPP)$_m$ electrodes were mainly attributed to the enhanced charge transfer by the MnPP ligands. Additionally, these results could be also supported by the EIS measurements, showing that the R$_{ct}$ of the (Fe$_3$O$_4$ NP/MnPP/ITO NP/MnPP)$_{20}$ electrode (~5.0 Ω) was significantly lower than that of the (Fe$_3$O$_4$ NP/PAA/ITO NP/PAA)$_{20}$ electrode (~31.7 Ω) (Fig. 3e).

Another notable advantage of our approach is that the MnPP-mediated assembly can produce the densely and homogeneously NP-packed structure that can maximize the volumetric capacitance (C$_{vol}$) of electrodes. The (Fe$_3$O$_4$ NP/MnPP/ITO NP/MnPP)$_m$ electrodes with a high mass density of approximately 2.9 g cm^{-3} showed a high C$_{vol}$ of ~367.6 mF cm^{-3} (for $m = 20$), which was almost independent of the film thickness (C$_{vol}$ of ~369.5 mF cm^{-3} for $m = 5$) in the range from ~65 to 244 nm (Fig. S25). These results demonstrated that the volumetric energy performance of TMO NP-based electrodes could be significantly improved through the efficient structural design of MnPP-mediated electrodes. Furthermore, it should be noted that the MnPP ligands enabled the formation of a robust electrode structure based on the strong coordination bonding for the bare surface of oxide NPs. Therefore, the (Fe$_3$O$_4$ NP/MnPP/ITO NP/MnPP)$_{20}$ electrode could exhibit an excellent capacitance retention of ~88 % with a good Coulombic efficiency of ~99 % after 5000 GCD cycles at a current density of 0.5 mA cm^{-2}, maintaining its structural integrity (Fig. 3f and Fig. S26).

2.3. Electrochemical properties of MnPP-mediated multilayer-coated textile electrodes

Although the densely packed thin film-type electrodes proposed in the present study possess the fascinating characteristics for realizing high-efficiency and/or high-power energy storage performance, the relatively low mass loading of active components makes it difficult to achieve higher energy density [54]. To overcome this drawback, the (Fe$_3$O$_4$ NP/MnPP/ITO NP/MnPP)$_m$ multilayers were deposited onto porous TCC with extremely large surface area (Fig. 4a), which were prepared through the LbL assembly of metal NPs and subsequent Ni electroplating as reported in our previous paper [55]. In this case, the electroplated Ni layer was homogeneously deposited onto all fibrils of a metal NP-coated cotton textile (Fig. S27). The formed 780 μm-thick TCC
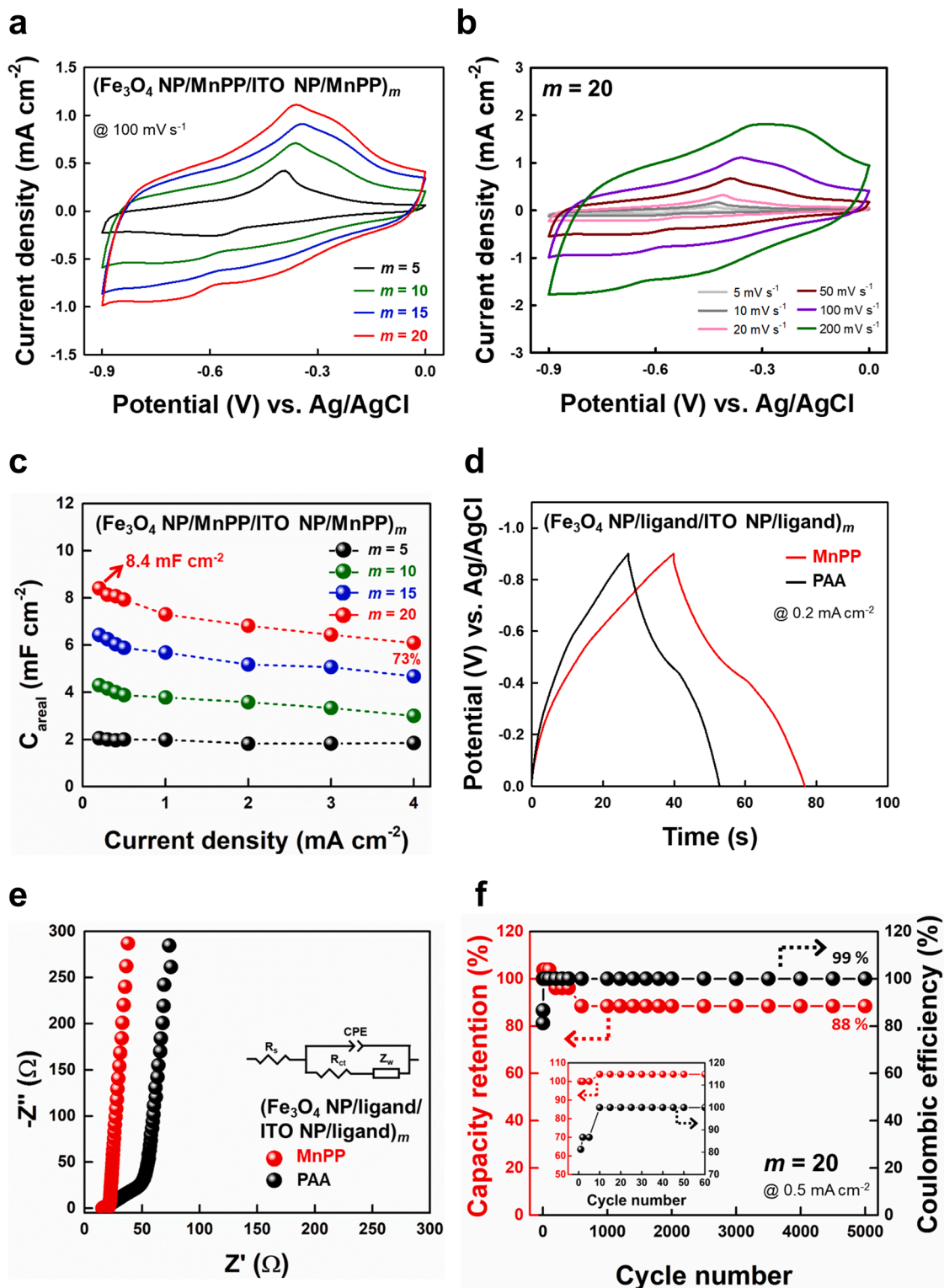
Fig. 3. (a) CV curves of (Fe$_3$O$_4$ NP/MnPP/ITO NP/MnPP)$_m$ electrodes with increasing the periodic number from 5 to 20 at a scan rate of 100 mV s^{-1}. (b) Scan rate-dependent CV curves of (Fe$_3$O$_4$ NP/MnPP/ITO NP/MnPP)$_{20}$ electrode in the range of scan rate from 5 to 200 mV s^{-1}. (c) C$_{areal}$ of (Fe$_3$O$_4$ NP/MnPP/ITO NP/MnPP)$_m$ electrodes with different periodic numbers obtained from the GCD curves with increasing the current density from 0.2 to 4.0 mA cm^{-2}. (d) GCD curves (at a current density of 0.2 mA cm^{-2}) and (e) Nyquist plots of (Fe$_3$O$_4$ NP/ligand/ITO NP/ligand)$_{20}$ electrodes (ligand: MnPP and PAA). (f) Capacity retention (left axis, red circles) and Coulombic efficiency (right axis, black circles) of (Fe$_3$O$_4$ NP/MnPP/ITO NP/MnPP)$_{20}$ electrode during 5000 GCD cycles at a current density of 0.5 mA cm^{-2}. (For interpretation of the references to colour in this figure legend, the reader is referred to the web version of this article.)
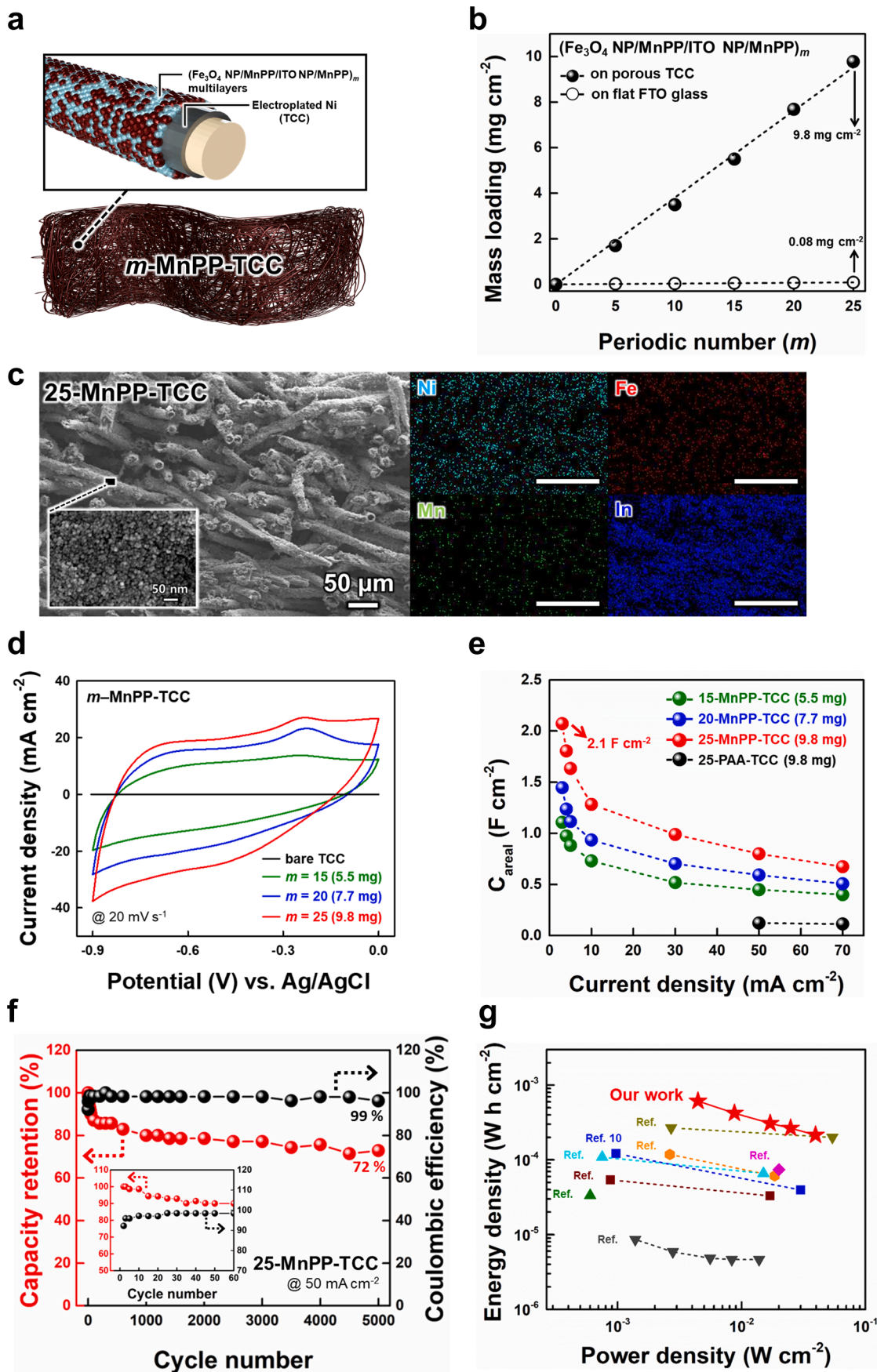
(caption on next page)

Fig. 4. (a) Schematic diagram of (Fe$_3$O$_4$ NP/MnPP/ITO NP/MnPP)$_m$ multilayers deposited onto a 3D porous TCC. (b) Comparison of mass loading of (Fe$_3$O$_4$ NP/MnPP/ITO NP/MnPP)$_m$ multilayers between on porous TCC and on flat FTO glass with increasing the periodic number from 5 to 25. (c) Cross-sectional/planar FE-SEM and corresponding EDS elemental mapping images of 25-MnPP-TCC. (d) CV curves of m-MnPP-TCCs with different periodic numbers and bare TCC at a scan rate of 20 mV s^{-1}. (e) C$_{areal}$ of m-MnPP-TCCs with different periodic numbers and 25-PAA-TCC as the current density increases from 3.0 to 70 mA cm^{-2}. (f) Capacity retention (left axis, red circles) and Coulombic efficiency (right axis, black circles) of 25-MnPP-TCC during 5000 GCD cycles at a current density of 50 mA cm^{-2}. (g) Ragone plot (as a function of areal energy/power densities) of the 25-MnPP-TCC//CT compared with previously reported asymmetric pseudocapacitors. (For interpretation of the references to colour in this figure legend, the reader is referred to the web version of this article.)

exhibited a total mass density of ~0.81 g cm^{-3} (mass density of bare cotton textile: ~0.22 g cm^{-3}), an extremely low sheet resistance of ~0.02 Ω sq^{-1}, and a large specific surface area of ~6.50 m^2 g^{-1} (confirmed by the mercury intrusion porosimetry). As shown in Fig. 4b, the mass loading of (Fe$_3$O$_4$ NP/MnPP/ITO NP/MnPP)$_m$ multilayers on the TCC (i.e., m-MnPP-TCC) was increased linearly from ~1.5 ($m = 5$) to 9.8 mg cm^{-2} ($m = 25$), which was ~120 times higher than that on the nonporous flat current collector (i.e., FTO glass). Additionally, FE-SEM and EDS mapping images clearly showed that these multilayers were uniformly coated onto all regions ranging from the exterior to the interior of highly porous 3D TCC without any notable aggregation of components (Fig. 4c). In particular, another promising feature of our approach was the fact that the deposited multilayers still maintained their densely NP-packed structure despite the tremendous increase in the mass loading of active components, which could be highly advantageous for favorable rate capability and high energy efficiency.

To confirm whether the substantially increased surface area of TCCs could be efficiently utilized for the electrochemical reaction, we calculated the electrochemical surface area (ECSA) from the double-layer capacitances (C$_{dl}$) obtained in the scan rate-dependent CV curves (Fig. S28). The CV scans were recorded in the non-Faradaic potential region ranging from −0.1 to 0 V at different scan rates ranging from 10 to 50 mV s^{-1}. In this case, the measured ECSA of 25-MnPP-TCC was nearly 254 times higher than that of flat (Fe$_3$O$_4$ NP/MnPP/ITO NP/MnPP)$_{20}$ electrode, evidently implying the enlarged surface area of porous TCCs. The CV curves of m-MnPP-TCCs displayed the typical pseudocapacitive features with high current responses and large CV area, which also regularly increased with increasing the periodic number (or mass loading) from 15 (~5.5 mg cm^{-2}) to 25 (~9.8 mg cm^{-2}) (Fig. 4d and Fig. S29). However, this behavior was in stark contrast to that of (Fe$_3$O$_4$ NP/PAA/ITO NP/PAA)$_{25}$ multilayer-coated TCC (i.e., 25-PAA-TCC) with a significantly distorted CV shape despite the same mass loading (~9.8 mg cm^{-2}) (Fig. S30). Additionally, the GCD profiles with quasi-triangular shapes of m-MnPP-TCCs implied stable charge storage behaviors (Fig. S31). In this case, the 25-MnPP-TCC exhibited a maximum C$_{areal}$ of ~2.1 F cm^{-2} at a current density of 3.0 mA cm^{-2} with a high Coulombic efficiency of ~98 %, outperforming previously reported Fe$_3$O$_4$-based electrodes (Fig. 4e and Table S1). On the other hand, the GCD profile of 25-PAA-TCC showed a plateau in a high voltage region at a current density lower than 50 mA cm^{-2} during the charging step (Fig. S32), mainly caused by the irreversible current consumption such as electrolyte decomposition [56,57]. This phenomenon implied that the insulating PAA ligands severely limited the charge transfer kinetics at the high mass loading of electrodes. As a result, the 25-PAA-TCC showed a much lower C$_{areal}$ (~0.13 F cm^{-2}) at a current density of 50 mA cm^{-2} than that of the 25-MnPP-TCC (~0.80 F cm^{-2}), with a low Coulombic efficiency of ~58 % (Fig. S33). This large difference in the energy efficiency implied that the ligand-induced charge transfer effects could be more intensified at higher mass loading of active materials on the porous TCCs, compared to the case of flat electrodes. The enhanced charge transfer of m-MnPP-TCCs was further confirmed by the EIS results that the R$_{ct}$ of 25-MnPP-TCC (~1.8 Ω) was much lower than that of 25-PAA-TCC (~14.5 Ω) (Fig. S34). That is, the 25-PAA-TCC could not effectively utilize the structural advantages of TCC with large surface area due to the presence of polymeric ligands with insulating properties. On the other hand, the MnPP ligands adsorbed onto all surface of NPs could provide an efficient pathway for charge transport and a favorable electrolyte reservoir. As a result, the 25-MnPP-TCC maintained ~72 %

of its initial capacitance with a high Coulombic efficiency of ~99 % after 5000 GCD cycles at a current density of 50 mA cm^{-2} in spite of the high mass loading of ~9.8 mg cm^{-2} (Fig. 4f), which was mainly attributed to the formation of favorable and robust interfacial bonding between neighboring NPs bridged by the MnPP ligands.

Additionally, in order to confirm the possibility for applying the m-MnPP-TCCs to asymmetric pseudocapacitors, we constructed a full-cell system composed of 25-MnPP-TCC as a negative electrode and carbon textile (CT) as a positive electrode (i.e., 25-MnPP-TCC//CT) using a 1.0 M Na$_2$SO$_4$ electrolyte. In this case, the positive CT electrode displayed a stable EDLC behavior in the potential window of 0–0.9 V (vs Ag/AgCl) (Fig. S35a), and its total charge amount was equally balanced with the counter 25-MnPP-TCC electrode. As a result, the overall potential window of 25-MnPP-TCC//CT device could be successfully extended up to 1.8 V (Fig. S35b), which was also identified from stable charging/discharging behaviors in the scan rate-dependent CV and the current density-dependent GCD curves (Fig. S35c-S35d). In this case, the areal energy and power densities of 25-MnPP-TCC//CT were calculated to be ~613 μW h cm^{-2} and ~39.5 mW cm^{-2}, respectively, outperforming the previously reported studies using Fe$_3$O$_4$ as an active material (Fig. 4g and Table S2). These results evidently demonstrated that the MnPP ligands, which can directly bridge the interfaces between high-energy TMO NPs and conductive NPs, have significant impacts on the overall energy storage performance, and furthermore, that the better understanding of these ligand effects become increasingly important in developing high-performance energy storage electrodes.

3. Conclusion

In this study, we demonstrated that the overall electrochemical performance of TMO NP-based pseudocapacitor electrodes could be significantly improved by the redox-active ligand (i.e., MnPP ligand)-mediated LbL assembly based on the well-defined interfacial interactions. Our approach highlighted that the ligand design of TMO NPs could have a significant effect on the charge transfer kinetics within the electrode, and furthermore it could provide an optimal electrode structure for realizing high-performance energy storage electrodes that require high energy/power densities and rate capability. The MnPP ligands were LbL-assembled with high-energy Fe$_3$O$_4$ and conductive ITO NPs, effectively eliminating the electrochemically inactive native ligands as well as directly and robustly bridging the interface between neighboring NPs without the use of polymeric binders. Owing to this effective replacement of inactive/insulating organic species with electrochemically active MnPP ligands, the resultant TMO NP-based electrodes could exhibit a higher capacity and more facile charge transfer than insulating polymeric ligand-mediated electrodes, even at high electrode packing density. Particularly, in the case of using porous TCCs with large surface area instead of flat current collectors, the electrochemically active effect of MnPP ligands on the overall energy storage performance of TMO NP-based electrodes could be more clearly observed. Note that the high mass loading of active TMO NPs could be easily applied to textile electrodes without sacrificing the charge transfer kinetics within the electrodes. Considering that the redox-active MnPP-mediated LbL assembly is based on effective control of the ligand type, interfacial interactions, and structural design within the electrodes, we believe that our approach can provide a basis for developing and designing high-performance energy storage devices.

Declaration of Competing Interest

The authors declare that they have no known competing financial interests or personal relationships that could have appeared to influence the work reported in this paper.

Data availability

The authors do not have permission to share data.

Acknowledgments

Appendix A. Supplementary data

Supplementary data to this article can be found online at https://doi.org/10.1016/j.cej.2022.140742.

References

[1] P. Simon, Y. Gogotsi, B. Dunn, Where do batteries end and supercapacitors begin? Science 434 (2014) 1210–1211, https://doi.org/10.1126/science.1249625.

[2] A. Noori, M.F. El-Kady, M.S. Rahmanifar, R.B. Kaner, M.F. Mousavi, Towards establishing standard performance metrics for batteries, supercapacitors and beyond, Chem. Soc. Rev. 48 (2019) 1272–1341, https://doi.org/10.1039/c8cs00581h.

[3] M. Huang, X. Wang, X. Liu, L. Mai, Fast ionic storage in aqueous rechargeable batteries: from fundamentals to applications, Adv. Mater. 34 (2022) 2105611, https://doi.org/10.1002/adma.202105611.

[4] T. Brezesinski, J. Wang, S.H. Tolbert, B. Dunn, Ordered mesoporous α-MoO3 with iso-oriented nanocrystalline walls for thin-film pseudocapacitors, Nat. Mater. 9 (2010) 146–151, https://doi.org/10.1038/NMAT2612.

[5] J.B. Goodenough, Y. Kim, Challenges for rechargeable Li batteries, Chem. Mater. 12 (2010) 587–603, https://doi.org/10.1021/cm901452z.

[6] Y. Kuang, C. Chen, D. Kirsch, L. Hu, Thick electrode batteries: principles, opportunities, and challenges, Adv. Energy. Mater. 9 (2019) 1901457, https://doi.org/10.1002/aenm.201901457.

[7] M.R. Lukatskaya, B. Dunn, Y. Gogotsi, Multidimensional materials and device architectures for future hybrid energy storage, Nat. Commun. 7 (2016) 12647, https://doi.org/10.1038/ncomms12647.

[8] V. Augustyn, P. Simon, B. Dunn, Pseudocapacitive oxide materials for high-rate electrochemical energy storage, Energy Environ. Sci. 7 (2014) 1597–1614, https://doi.org/10.1039/c3ee44164d.

[9] C. Choi, D.S. Ashby, D.M. Butts, R.H. DeBlock, Q. Wei, J. Lau, B. Dunn, Achieving high energy density and high power density with pseudocapacitive materials, Nat. Rev. Mater. 5 (2020) 5–19, https://doi.org/10.1038/s41578-019-0142-z.

[10] E. Pomerantseva, F. Bonaccorso, X. Feng, Y. Cui, Y. Gogotsi, Energy storage: The future enabled by nanomaterials, Science 366 (2019) eaan8285, 10.1126/science.aan8285.

[11] Y. Ko, M. Kwon, W.K. Bae, B. Lee, S.W. Lee, J. Cho, Flexible supercapacitor electrodes based on real metal-like cellulose papers, Nat. Commun. 8 (2017) 536, https://doi.org/10.1038/s41467-017-00550-3.

[12] Z. Yu, L. Tetard, L. Zhai, J. Thomas, Supercapacitor electrode materials: nanostructures from 0 to 3 dimensions, Energy Environ. Sci. 8 (2015) 702–730, https://doi.org/10.1039/c4ee03229b.

[13] J. Jiang, Y. Li, J. Liu, X. Huang, C. Yuan, X.W. Lou, Recent advances in metal oxide-based electrode architecture design for electrochemical energy storage, Adv. Mater. 24 (2012) 5166–5180, https://doi.org/10.1002/adma.201202146.

[14] Y. Ko, C.H. Kwon, S.W. Lee, J. Cho, Nanoparticle-based electrodes with high charge transfer efficiency through ligand exchange layer-by-layer assembly, Adv. Mater. 32 (2020) 2001924, https://doi.org/10.1002/adma.202001924.

[15] J. Kang, S. Zhang, Z. Zhang, Three-dimensional binder-free nanoarchitectures for advanced pseudocapacitors, Adv. Mater. 29 (2017) 1700515, https://doi.org/10.1002/adma.201700515.

[16] J. Ni, X. Zhu, Y. Yuan, Z. Wang, Y. Li, L. Ma, A. Dai, M. Li, T. Wu, R. Shahbazian-Yassar, J. Lu, L. Li, Rooting binder-free tin nanoarrays into copper substrate via tin-copper alloying for robust energy storage, Nat. Commun. 11 (2020) 1212, https://doi.org/10.1038/s41467-020-15045-x.

[17] T. Jin, Q. Han, L. Jiao, Binder-free electrodes for advanced sodium-ion batteries, Adv. Mater. 32 (2020) 1806304, https://doi.org/10.1002/adma.201806304.

[18] W. Ma, W. Li, M. Li, Q. Mao, Z. Pan, J. Hu, X. Li, M. Zhu, Y. Zhang, Unzipped carbon nanotube/graphene hybrid fiber with less "dead volume" for ultrahigh volumetric energy density supercapacitors, Adv. Funct. Mater. 31 (2021) 2100195, https://doi.org/10.1002/adfm.202100195.

[19] Y. Lin, X. Wang, G. Qian, J.J. Watkins, Additive-driven self-assembly of well-ordered mesoporous carbon/iron oxide nanoparticle composites for

[20] F. Xu, H. Xu, X. Chen, D. Wu, Y. Wu, H. Liu, C. Gu, R. Fu, D. Jiang, A porphyrin complex as a self-conditioned electrode material for high-performance energy storage, Angew. Chem. 127 (2015) 10341–10346, https://doi.org/10.1002/anie.201702805.

[21] H. Zhang, Y. Zhang, C. Gu, Y. Ma, Electropolymerized conjugated microporous poly(zinc-porphyrin) films as potential electrode materials in supercapacitors, Adv. Energy Mater. 5 (2015) 1402175, https://doi.org/10.1002/aenm.201402175.

[22] F. Cao, M. Zhao, Y. Yu, B. Chen, Y. Huang, J. Yang, X. Cao, Q. Lu, X. Zhang, Z. Zhang, C. Tan, H. Zhang, Synthesis of two-dimensional CoS1.097/nitrogen-doped carbon nanocomposites using metal−organic framework nanosheets as precursors for supercapacitor application, J. Am. Chem. Soc. 138 (2016) 6924–6927, https://doi.org/10.1021/jacs.6b02540.

[23] K. Jeong, J.-M. Kim, S.H. Kim, G. Y. Jung, J. Yoo, S.-H. Kim, S. K. Kwak, S.-Y, Lee, Carbon-nanotube-cored cobalt porphyrin as a 1D nanohybrid strategy for high-performance lithium-ion battery anodes, Adv. Funct. Mater. 29 (2019) 1806937, 10.1002/adfm.201806937.

[24] W. Zhao, J. Peng, W. Wang, B. Jin, T. Chen, S. Liu, Q. Zhao, W. Huang, Interlayer hydrogen-bonded metal porphyrin frameworks/MXene hybrid film with high capacitance for flexible all-solid-state supercapacitors, Small 15 (2019) 1901351, https://doi.org/10.1002/smll.201901351.

[25] H. Yao, F. Zhang, G. Zhang, H. Luo, L. Liu, M. Shen, Y. Yang, A novel two-dimensional coordination polymer-polypyrrole hybrid material as a high-performance electrode for flexible supercapacitor, Chem. Eng. J. 334 (2018) 2547–2557, https://doi.org/10.1016/j.cej.2017.12.013.

[26] H.-G. Wang, C. Jiang, C. Yuan, Q. Wu, Q. Li, Q. Duan, Complexing agent engineered strategy for anchoring SnO2 nanoparticles on sulfur/nitrogen co-doped graphene for superior lithium and sodium ion storage, Chem. Eng. J. 332 (2018) 237–244, https://doi.org/10.1016/j.cej.2017.09.081.

[27] A.C. Lim, H.J. Kwon, H.S. Jadhav, J.G. Seo, Porphyrin-stabilized CNT in nanofiber via non-covalent interaction for enhanced electrochemical performance, Electrochim. Acta 274 (2018) 112–120, https://doi.org/10.1016/j.electacta.2018.04.064.

[28] F. Xu, H. Xu, X. Chen, D. Wu, Y. Wu, H. Liu, C. Gu, R. Fu, D. Jiang, Radical covalent organic frameworks: a general strategy to immobilize open-accessible polyradicals for high-performance capacitive energy storage, Angew. Chem. Int. Ed. 127 (2015) 6918–6922, https://doi.org/10.1002/ange.201501706.

[29] A. Kumar, D. Sarkar, S. Mukherjee, S. Patil, D.D. Sarma, A. Shukla, Realizing an asymmetric supercapacitor employing carbon nanotubes anchored to Mn3O4 cathode and Fe3O4 anode, ACS Appl. Mater. Interfaces 10 (2018) 42484–42493, https://doi.org/10.1021/acsami.8b16639.

[30] N. Jabeen, A. Hussain, Q. Xia, S. Sun, J. Zhum, H. Xia, High-performance 2.6 V aqueous asymmetric supercapacitors based on in situ formed Na0.5MnO2 nanosheet assembled nanowall arrays, Adv. Mater. 29 (2017) 1700804, 10.1002/adma.201700804.

[31] C. Zhao, X. Shao, Y. Zhang, X. Qian, Fe2O3/reduced graphene oxide/Fe3O4 composite in situ grown on Fe foil for high-performance supercapacitors, ACS Appl. Mater. Interfaces 8 (2016) 30133–30142, https://doi.org/10.1021/acsami.6b09594.

[32] J. Sun, Y. Huang, C. Fu, Y. Huang, M. Zhu, X. Tao, C. Zhi, H. Hu, A high performance fiber-shaped PEDOT@MnO2//C@Fe3O4 asymmetric supercapacitor for wearable electronics, J. Mater. Chem. A 4 (2016) 14877–14883, https://doi.org/10.1039/C6TA05898A.

[33] Z. Sun, X. Cai, Y. Song, X. Liu, Electrochemical deposition of honeycomb magnetite on partially exfoliated graphite as anode for capacitive applications, J. Power Sources 359 (2017) 57–63, https://doi.org/10.1016/j.jpowsour.2017.05.055.

[34] L. Li, C. Jia, Z. Shao, J. Wang, F. Wang, W. Wang, H. Hang, D. Zu, H. Wu, Fe3O4/nitrogen-doped carbon electrodes from tailored thermal expansion toward flexible solid-state asymmetric supercapacitors, Adv. Mater. Interfaces 6 (2019) 1901250, https://doi.org/10.1002/admi.201901250.

[35] J. Zhu, L. Huang, Y. Xiao, L. Shen, Q. Chen, W. Shi, Hydrogenated CoOx nanowire@Ni(OH)2 nanosheet core–shell nanostructures for high-performance asymmetric supercapacitors, Nanoscale 6 (2014) 6772–6781, https://doi.org/10.1039/C4NR00771A.

[36] M. Guo, J. Balamurugan, X. Li, N.H. Kim, J.H. Lee, Hierarchical 3D cobalt-doped Fe3O4 nanospheres@NG hybrid as an advanced anode material for high-performance asymmetric supercapacitors, Small 13 (2017) 1701275, https://doi.org/10.1002/smll.201701275.

[37] R.D. Arasasingham, T.C. Bruice, Reaction of hydroxide ion with manganese (III) tetramesitylporphyrins and the oxidation states of manganese tetramesitylporphyrins, J. Am. Chem. Soc. 29 (1990) 1422–1427, https://doi.org/10.1021/ic00332a028.

[38] G. Golubkov, J. Bendix, H.B. Gray, A. Mahammed, I. Goldberg, A.J. DiBilio, Z. Gross, High-valent manganese corroles and the first perhalogenated metallocorrole catalyst, Angew. Chem. Int. Ed. 40 (2001) 2132–2134, https://doi.org/10.1002/1521-3773(20010601)40:11<2132::AID-ANIE2132>3.0.CO;2-5.

[39] W. Zhang, W. Lai, R. Cao, Energy-related small molecule activation reactions: oxygen reduction and hydrogen and oxygen evolution reactions catalyzed by porphyrin- and corrole-based systems, Chem. Rev. 117 (2017) 3717–3797, https://doi.org/10.1021/acs.chemrev.6b00299.

[40] M.-S. Liao, S. Scheiner, Electronic structure and bonding in metal porphyrins, metal=Fe Co, Ni, Cu, Zn, J. Chem. Phys. 117 (2002) 205, https://doi.org/10.1063/1.1480872.

[41] S. Sun, H. Zeng, D.B. Robinson, S. Raous, P.M. Rice, S.X. Wang, G. Li, Monodisperse MFe2O4 (M = Fe Co, Mn) nanoparticles, J. Am. Chem. Soc. 126 (2004) 273–279, https://doi.org/10.1021/ja0380852.

[42] I. Cho, Y. Song, S. Cheong, Y. Kim, J. Cho, Layer-by-layer assembled oxide nanoparticle electrodes with high transparency, electrical conductivity, and electrochemical activity by reducing organic linker-induced oxygen vacancies, Small 16 (2020) 1906768, https://doi.org/10.1002/smll.201906768.

[43] J.W. Kim, V. Augustyn, B. Dunn, The effect of crystallinity on the rapid pseudocapacitive response of Nb_2O_5, Adv. Energy Mater. 2 (2012) 141–148, https://doi.org/10.1002/aenm.201100494.

[44] P. Poizot, S. Laruelle, S. Grugeon, L. Dupoint, J.-M. Tarascon, Nano-sized transition-metal oxides as negative-electrode materials for lithium-ion batteries, Nature 407 (2020) 496–499, https://doi.org/10.1038/35035045.

[45] L.J. Boucher, J.J. Katz, The infrared spectra of metalloporphyrins (4000–160 cm^{-1}), J. Am. Chem. Soc. 89 (1966) 1340–1345, https://doi.org/10.1021/ja00982a011.

[46] S. Sun, Recent advances in chemical synthesis, self-assembly, and applications of FePt nanoparticles, Adv. Mater. 18 (2006) 393–403, https://doi.org/10.1002/adma.200501464.

[47] B.C. Mei, K. Susumu, I.L. Medintz, H. Mattoussi, Polyethylene glycol-based bidentate ligands to enhance quantum dot and gold nanoparticle stability in biological media, Nat. Protoc. 4 (2009) 412–423, https://doi.org/10.1038/nprot.2008.243.

[48] J.-M. Lim, S. Kim, N.S. Luu, J.R. Downing, M.T.Z. Tan, K.-Y. Park, J.C. Hechter, J. C. Hechter, V.P. Dravid, K. He, M.C. Hersam, High volumetric energy and power density Li_2TiSiO_5 battery anodes via graphene functionalization, Matter 3 (2020) 522–533, https://doi.org/10.1016/j.matt.2020.07.017.

[49] N. Liu, Z. Lu, J. Zhao, M.T. McDowell, H.-W. Lee, W. Zhao, Y. Cui, A pomegranate-inspired nanoscale design for large-volume-change lithium battery anodes, Nat. Nanotechnol. 9 (2014) 187–192, https://doi.org/10.1038/NNANO.2014.6.

[50] S. Bellani, L. Najafi, G. Tullii, A. Ansaldo, R. Oropesa-Nuñez, M. Pratom, M. Colombo, M.R. Antognazza, F. Bonaccorso, ITO nanoparticles break optical transparency/high-areal capacitance trade-off for advanced aqueous supercapacitors, J. Mater. Chem. A 5 (2017) 25177–25186, https://doi.org/10.1039/c7ta09220brs.

[51] V.D. Nithya, N.S. Arul, Progress and development of Fe_3O_4 electrodes for supercapacitors, J. Mater. Chem. A 4 (2016) 10767–10778, https://doi.org/10.1039/c6ta02582j.

[52] A. Friedman, L. Landau, S. Gone, Z. Gross, L. Elbaz, Efficient bio-inspired oxygen reduction electrocatalysis with electropolymerized cobalt corroles, ACS Catal. 8 (2018) 5024–5031, https://doi.org/10.1021/acscatal.8b00876.

[53] M. Lucero, G. Ramırez, A. Riquelme, I. Azocar, M. Isaacs, F. Armijo, J.E. Forster, E. Trollund, M.J. Aguirre, D. Lexa, Electrocatalytic oxidation of sulfite at polymeric iron tetra (4-aminophenyl) porphyrin—modified electrode, J. Mol. Catal. A Chem. 221 (2004) 71–76, https://doi.org/10.1016/j.molcata.2004.04.045.

[54] Y. Gogotsi, P. Simon, True performance metrics in electrochemical energy storage, Science 334 (2011) 6058, https://doi.org/10.1126/science.1213003.

[55] S. Woo, D. Nam, W. Chang, Y. Ko, S. Lee, Y. Song, B. Yeom, J.H. Moon, S.W. Lee, J. Cho, A Layer-by-layer assembly route to electroplated fibril-based 3D porous current collectors for energy storage devices, Small 17 (2021) 2007579, https://doi.org/10.1002/smll.202007579.

[56] S. Ban, J. Zhang, L. Zhang, K. Tsay, D. Song, X. Zou, Charging and discharging electrochemical supercapacitors in the presence of both parallel leakage process and electrochemical decomposition of solvent, Electrochim. Acta 90 (2013) 542–549, https://doi.org/10.1016/j.electacta.2012.12.056.

[57] L. Chen, H. Bai, Z. Huang, L. Li, Mechanism investigation and suppression of self-discharge in active electrolyte enhanced supercapacitors, Energy Environ. Sci. 7 (2014) 1750–1759, https://doi.org/10.1039/c4ee00002a.